Ag$_2$CO$_3$-halloysite nanotubes composite with enhanced removal efficiency for water soluble dyes

Emmanuel Nyankson, Benjamin Agyei-Tuffour, Ebenezer Annan, Abu Yaya, Bismark Mensah, Boateng Onwona-Agyeman, Reuben Amedalor, Benson Kwaku-Frimpong, Johnson Kwame Efavi [*]

Materials Science and Engineering Department, University of Ghana, P.O. Box LG 77, Accra, Ghana

ABSTRACT

The release of water soluble dyes into the environment is an utmost concern in many countries. This paper presents the effects of Ag$_2$CO$_3$-halloysite composites on the efficient removal of water soluble dyes. In this study, NaHCO$_3$ solution was added dropwisely to halloysite nanotubes (HNTs) dispersed in aqueous AgNO$_3$ to form Ag$_2$CO$_3$-HNTs composite. The synthesized Ag$_2$CO$_3$-HNTs composite was characterized with Diffused Reflectance Spectroscopy (DRS), X-ray Diffraction (XRD), Thermogravimetric analysis (TGA), Scanning Electron Microscopy-Energy Dispersive Spectroscopy (SEM-EDX) and Fourier Transform Infra-Red (FT-IR) spectroscopy. The photocatalytic activity and the adsorption capacity of Ag$_2$CO$_3$-HNTs on methylene blue and rhodamine b dyes were dependent on pH and the amount of HNTs used in the synthesis. The photodegradation efficiency of Ag$_2$CO$_3$ was lower when compared with that of the composite material. This observation is due to the reduction in the electron-hole recombination with the HNTs acting as electron trapping site and the enhanced aqueous dispersity of Ag$_2$CO$_3$-HNTs. The enhanced adsorption of water soluble dyes by the Ag$_2$CO$_3$-HNTs resulted from the electrostatic attraction of cationic dyes to the surface of the HNTs (negatively charged). The Ag$_2$CO$_3$-HNTs therefore removed dye pollutants through a combination of photocatalytic and adsorption processes. The results obtained during the study confirmed the potential application of Ag$_2$CO$_3$-HNTs composite in water treatment technologies.

1. Introduction

Water pollution by water soluble dyes is a major challenge being battled by the environmental protection agencies worldwide as a result of the industrial dye effluents been discharged into existing water bodies. Although synthetic dyes are important coloring agent used for various applications in the textile, paper, food processing, leather tanning, cosmetics and plastic industries [1], their release into water bodies however, gives these water bodies an undesirable color, prevents sunlight penetration and influences photo and biological activities in the aquatic environment [2]. The release of large volumes of water soluble dyes into the environment therefore has a consequential effect on aquatic species and the populace. Different remediation strategies like membrane separation, advanced oxidation, coagulation, and adsorption have been employed to reduce the effect of dyes on the environment [3].

The potential usage of photocatalysis in contaminated water treatment technologies has been investigated my many researchers. Semiconductor photocatalysis involves the absorption of light by a semiconductor, the transfer of electrons from the valence band (VB) to the conduction band (CB) of the semiconductor generating an electron-hole pair, and the transfer of these charge carriers to the surface of the semiconductor to be used in the oxidation of organic contaminants and the creation of reactive oxygen species (ROS) [4]. The most widely investigated photocatalyst is TiO$_2$. With a band gap of ca. 3.0–3.2 eV, TiO$_2$ absorbs only ultraviolet light limiting its potential applications [5]. Therefore, the focus of most researchers has been to develop highly efficient photocatalyst that are active in the visible light. This research effort has led to the discovery of silver based photocatalyst such as Ag$_3$PO$_4$ [6], Ag$_2$O [7], AgCl [8], AgBr [9] and Ag$_2$CO$_3$ [10] as the new generation of visible light active photocatalyst. Ag$_2$CO$_3$ photocatalyst has been reported to be very effective in degrading water soluble dyes [11, 12].

Combination of photocatalysis with other water-soluble dye remediating strategied may result in enhanced overall dye removal efficiency. One naturally occurring aluminosilicate clay material that has been reported to possess excellent adsorption property is halloysite nanotubes

---

(HNTs), which has a chemical formula $Al_2Si_2O_5(OH)_4 \cdot nH_2O$. The rolling structure of halloysite nanotubes results from the misfit between the bond length of Si–O and Al–O present in HNTs [13, 14]. Halloysite nanotubes can be hydrated $(10\dot{A})$ or dehydrated $(7\dot{A})$. The structural features of dehydrated HNTs have recently been investigated and modelled [15]. The length of halloysite nanotubes has been reported to be between 0.5 – 1.5 μm while the size of the lumen is ca. 15–100 nm [16]. The outer and inner surfaces of halloysite nanotubes have opposite charges between pH values of 2–8. The potential application of HNTs are influenced by their properties which are in turn influenced by their geological origin. The HNTs used for this study were acquired from Sigma Aldrich, USA. The Sigma Aldrich HNTs is obtained from Dragon Mine deposit in Utah, North America. The specific surface area (BET) of the Sigma Aldrich HNTs has been reported to be 46.36 m^2/g [17]. Aluminosilicate halloysite nanotubes have found potential application in drug delivery [18], oil spill remediation [4, 19, 20] and water purification [21] due to their distinctive properties. The potential application of HNTs in removing water soluble dyes [21, 22, 23] has been examined. Luo Pentg et al. investigated the potential usage of HNTs in removing Neutral red from aqueous solution and reported an adsorption capacity of 12.5 and 53.7 mg/g at an HNTs dose of 0.4 and 0.05 g, respectively [22]. An adsorption capacity of between 40.81-82.78 mg/g has also been reported for the adsorption of methylene blue by HNTs [24]. Adsorption capacity values are dependent on initial dye concentration and HNTs dosage. Adsorption capacity values of 24.91 and 89.12 mg/g have been reported for the adsorption of methyl violet by HNTs [23]. Modification of HNTs may enhance the adsorption of pollutants. Modification of the lumen with anionic surfactants such as sodium dodecanoate and sodium dodecylsulfate has made it possible to adsorb apolar dyes such as Nile red within the lumen of HNTs [25]. In addition to dyes, HNTs have been utilized for the removal of the following toxic metals; Cr(VI) [26], Sb(V) [27] and Hg(II) [28].

Recovery of most photocatalyst after application is very challenging. This is due to their nanosized dimensions. Developing a supported photocatalyst system in which the support also serves as an adsorbent may enhance the efficiency of water treatment technologies. Adsorption of pollutants by HNTs will concentrate the pollutants near the surface of the Ag_2CO_3. This will reduce the diffusion path of pollutants towards the active sites on Ag_2CO_3 surface and maximize the contact between the pollutants, Ag_2CO_3 and photons. This photocatalyst-adsorbent system may find potential usage in water treatment technologies for the removal of water-soluble dyes, pesticides, pharmaceutical wastes, heavy metals and other harmful environmental pollutants.

To the best of the authors knowledge, a photocatalyst-adsorbent composite material made with halloysite nanotubes and Ag_2CO_3 has not been developed and investigated. In this work, Ag_2CO_3-Halloysite nanotube (Ag_2CO_3-HNTs) was developed and characterized with XRD, SEM-EDX, FTIR, TGA and DRS. The photocatalytic activity of Ag_2CO_3-HNTs in degrading rhodamine b and methylene blue dyes was examined. The effect of the weight percent of HNTs used in the synthesis on the photocatalytic activity was investigated. A detailed adsorption equilibrium studies was performed and fitted with Freundlich and Langmuir equilibrium isotherms. Kinetic data was also generated and fitted with pseudo second and first order adsorption kinetics model, and the interparticle diffusion model.

2. Experimental

Analytical graded Chemical reagents purchased from Sigma Aldrich, UK were utilized in this work without further purification.

2.1. Synthesis of Ag_2CO_3-halloysite nanotube (HNT) nanocomposite

In the synthesis of Ag_2CO_3-HNTs nanocomposite, a calculated amount of halloysite nanotubes were dispersed in 150 mL of 0.05 M AgNO$_3$ and sonicated for 30 mins. 153 mL of 0.2 M NaHCO$_3$ was then added dropwisely while stirring for 30 mins. The resulting solution was centrifuged to collect the precipitate. The precipitate was washed repeatedly (three cycles) with 1:1 v/v deionized water/ethanol solution and dried at room temperature to obtain Ag_2CO_3-HNT nanocomposite. Different amounts of HNT was used in the synthesis to obtain samples with 25 wt.%, 50 wt.% and 75 wt.% HNT, respectively. The procedure was repeated to obtain Ag_2CO_3 but without the addition of HNT.

2.2. Structural, thermal, microstructural and optical characterization of Ag_2CO_3-HNT composites

The phase composition of the synthesized Ag_2CO_3–HNT composite were obtained by X-ray Diffraction (Bruker D8 advanced focus diffractometer fitted with position sensitive detector (LynxEye) and standard detector, a Cu-Kα radiation and a 2Ө angular range of 10–80°).

The morphology of the synthesized nanocomposites was investigated with scanning electron microscopy (FEI Nova NanoSem) connected to EDX acquisition detector. The elemental composition was determined through EDX. The working distance used was between 4.2-5.9 mm and the energy of the beam was 5.0–20.0 kV.

FT-IR spectroscopy was performed to identify and confirm the functional groups present in the sample within the wavenumber 400-4000 cm^{-1}. The FTIR measurement was carried out using a Pike Miracle single-bound attenuated total reflectance (ATR) cell and ZnSe single crystal attached to the Bruker Tensor 2027 FT-IR spectrometer.

Thermogravimetric analysis of the Ag_2CO_3-HNT nanocomposite was carried out using TA Instruments Q500. The Analysis was performed under Nitrogen (flow rate of 60 mL/min and 40 mL/min for sample and balance, respectively) at the heating rate of 10 $°C/min$.

The DRS spectra of the samples were taken within the UV-VIS range using Ocean Optics UV-vis spectrophotometer. Prior to the analysis, the synthesized nanocomposites were placed between glass microscope slides and compressed into a flat film.

2.3. Adsorption studies

The adsorption capability of the synthesized nanocomposite was examined using methylene blue dye. 100 mg of Ag_2CO_3-50 wt.% HNT was added to 200 mL aqueous dye solution (2–10 mg/L). Samples of the dye solution were taken at specified time intervals and centrifuged at 6000 rpm for 5 mins to remove the powdered nanocomposite. The amount of the dye adsorbed was obtained by measuring the absorbance at 655 nm wavelength using the UV-VIS spectrometer.

2.4. Photodegradation of water soluble dyes

The photodegradation efficiency of Ag_2CO_3-HNT and Ag_2CO_3 was examined on rhodamine B and methylene blue dyes. In a typical photocatalytic degradation experiment, 200 mL of rhodamine B solution and 1 g/L catalyst concentration was used. A glass reactor with a quartz tube immersion well was used with illumination from 26 W Sylvania visible lamp. For each of the experiments, the solution was agitated in the dark for 30 mins to attain an adsorption-desorption equilibrium for illumination. 2 mL samples were taken at specific time intervals and centrifuged at 6000 rpm for 5 mins to remove the powdered photocatalyst. The absorbance of the water soluble dye was estimated using UV-VIS spectrometer. The absorbance was taken at a wavelength of 554 nm. A similar procedure was used to investigate the photodegradation of methylene blue dye. However, the absorbance values were taken at 665 nm and the starting concentration of methylene blue dye was 8 mg/L.

3. Results & discussion

3.1. Microstructural, optical and thermal analysis of Ag₂CO₃-HNT

The x-ray diffraction patterns of Ag₂CO₃, HNTs and Ag₂CO₃-HNTs composite are presented in Fig. 1. These patterns could be used to confirm the phase structure of the prepared Ag₂CO₃, HNTs and Ag₂CO₃-HNTs composite. The diffraction peaks of $2\theta = 18.55, 20.52, 32.61, 33.69, 37.08, 39.59, 41.75, 44.36, 47.11$ and 52.02 are indexed to pure monoclinic phase of Ag₂CO₃ and correspond to the crystallographic planes (020), (110), (-101), (-130), (200), (031), (220), (131), (230) and (150), respectively (JCPDS card number 26–0339) [29, 30, 31]. The intense diffraction peaks suggest the high crystallinity of Ag₂CO₃. Natural halloysite shows a characteristic peak at $2\theta = 20.1$ corresponding to the crystallographic plane (110). In addition, peaks were observed at 2θ values of 11.5 and 24.6 corresponding to the crystallographic planes of (001) and (002), respectively of HNTs. These peaks are characteristics of Sigma Aldrich HNTs which is obtained from the Dragon Mine at Utah, USA [17]. The other peaks observed is assigned to kaolinite [32]. The weak diffraction peaks of the HNTs suggest it has low crystallinity. The XRD patterns of the various formulations of the Ag₂CO₃-HNTs composite showed the characteristic peaks present in the pure Ag₂CO₃ and HNTs implying that no new phases were formed when the composite was synthesized. No impurity peak was found. The characteristic peak of HNTs (110) was visible in the composite with 75 wt.% HNTs. However, the (110) peak was not clearly visible in the samples with 50 and 25 wt.% HNTs. This may be attributed to the very high crystallinity of Ag₂CO₃ relative to that of HNTs. The very sharp peaks of the Ag₂CO₃ 'overshadowed' the low crystallinity peaks of HNTs. The presence of HNTs in the different formulations of the Ag₂CO₃-HNTs was confirmed by SEM, FTIR and TGA analysis.

The morphology of Ag₂CO₃, HNTs and Ag₂CO₃-HNTs composite was examined with SEM and is presented in Fig. 2. Ag₂CO₃ has rod-like shape as can be seen in Figs. 2(a) and 2(b) with average length of ~0.5–2 μm. At relatively lower magnification, Ag₂CO₃ showed smooth surface however when the magnification was increased to 10^5X, a rough surface can be seen (Fig. 2(b)). Such surface morphology may enhance dye adsorption and the migration of electrons on the surface of Ag₂CO₃ [33].

The cylindrical shape of the pure halloysite nanotubes is observed in Fig. 2(c). The surface of the HNTs is smooth. It is obvious from Fig. 2d that the HNTs were attached to the surface of the Ag₂CO₃ rods and the morphologies of both the Ag₂CO₃ and the HNTs did not change when the Ag₂CO₃-HNTs composite was formed. The EDX data presented in

Fig. 2(e) and (f) showed the presence of Al, Si, O, C and Ag. The Al and Si depicts the presence of HNTs which has the molecular formula Al₂Si₂(OH)4·nH₂O. The molar ratio of Al to Si is 1:1 and is confirmed in the EDX spectra. The EDX mapping showed an even distribution of the elements apart from a smaller portion that showed relatively higher concentrations of Ag.

The FT-IR spectra of Ag₂CO₃, HNTs and Ag₂CO₃-HNTs composite are presented in Fig. 3. The bands for the CO_3^{2-} present in the Ag₂CO₃ could be found at the wavenumbers 1420, 1319, 799 and 717 cm^{-1} [34]. The vibrational band occurring at 907 cm^{-1} was as a result of the deformation vibrations of hydroxyl groups at the inner surface of halloysite nanotubes whiles the vibrational peaks found at 3692 and 3622 cm^{-1} represents the vibrational stretching of the inner surface hydroxyl groups [16, 35, 36]. Also, the vibrational stretching of Si–O–Si group is represented by a band at 999 cm^{-1}. The peak located at 1068 cm^{-1} represents the vibrational stretching of the C–O group [37]. The vibrational band occurring at 1123 cm^{-1} and 1651 cm^{-1} was due to the epical stretching of the Si–O group and the vibrational deformation of the interlayer water, respectively. The FTIR spectra of the Ag₂CO₃-HNTs composite showed absorption bands which are combination of those of the pure Ag₂CO₃ and HNTS. However, there was a shift in the CO_3^{2-} bands at 1420, 1319 and 717 cm^{-1} to higher wavenumbers. The absorption band at 999 cm^{-1} also shifted to a higher wavenumber. This can be probably due to interactions between the Si–O–Si and CO_3^{2-} present in the HNTs and Ag₂CO₃, respectively and this influenced stretching vibrations of the Si–O–Si. In the composite materials, the C–O band in the Ag₂CO₃ was overshadowed by the intense Si–O–Si stretching vibration band of HNTs.

The TGA curves of the Ag₂CO₃, HNTs and Ag₂CO₃-HNTs composite are presented in Fig. 4. The TGA for the HNTs showed a gradual mass loss occurring between ca. 45–400 °C resulting from the decomposition of the adsorbed water found in the HNT. The dihydroxylation of HNT structure resulted in the abrupt mass loss at 400 °C [16]. On the other hand, Ag₂CO₃ decomposed through two distinct steps. The first decomposition occurred at ca. 180 °C and has been attributed to the decomposition of silver carbonate to form Ag₂O [38]. This decomposition was accompanied with ca. 15.5 % weight loss after which no weight loss was observed between ca. 240 and 430 °C. The weight loss (ca. 5.7 %) at 445 °C has been ascribed to the decomposition of Ag₂O to form Ag [38]. The two distinct decompositions for Ag₂CO₃ and HNTs were all observed in the TGA of the Ag₂CO₃-HNTs composite. The amount of the Ag₂CO₃ in Ag₂CO₃-HNTs was estimated using the rule of mixtures [39]. The calculation was done using the residual mass at 800 °C since complete degradation was observed in the TGA analysis at that temperature. The amount of the Ag₂CO₃ in the composite was estimated to be ca. 77 wt.%. This value is close to the amount (ca. 75 wt.%) used in the synthesis.

The UV-visible diffused reflectance spectroscopy of Ag₂CO₃ and Ag₂CO₃-HNTs are presented in Fig. 5. Ag₂CO₃ absorbs light in the UV and visible regions (absorption threshold of ca. 480 nm) of the solar spectrum. Addition of HNTs enhanced the absorption in the visible region. The optical bang gap energies were estimated from the Kubelka-Munk plots [40, 41] and presented in Table 1.

The estimated optical band gap of Ag₂CO₃ was 2.50 eV. This value is similar to those reported in literature [33]. The addition of HNTs showed no significant effect towards the optical band gap.

At zero charge, both the valence (E_{VB}) and conduction (E_{CB}) band edge potentials of Ag₂CO₃ were calculated using the formula [42]:

$$E_{VB} = X - E^e + 1.5E_g \tag{1}$$

$$E_{CB} = E_{VB} - E_g \tag{2}$$

E^e and E_g represent the energy of free electrons on the hydrogen scale and semiconductor band gap, respectively, the absolute electronegativity of the semiconductor (6.023 eV for Ag₂CO₃) was represented by X. E_{CB} and E_{VB} were cacluated to be 0.27 and 2.77 eV, respectively.
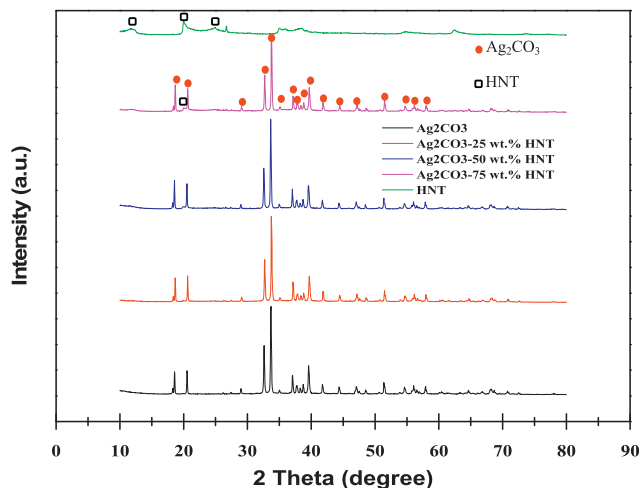

Fig. 1. XRD pattern for Ag₂CO₃, halloysite nanotubes (HNTs) and the different formulations of Ag₂CO₃-HNTs composite.
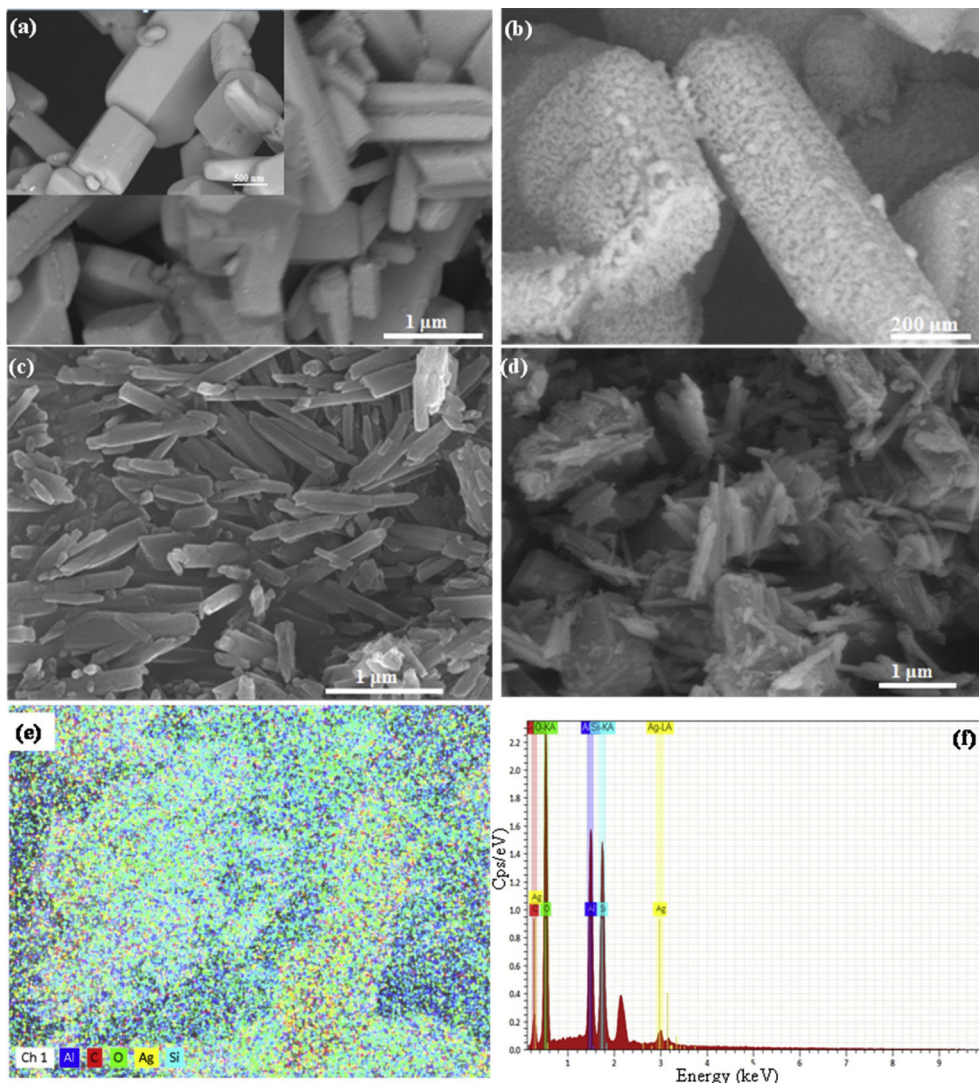
Fig. 2. The Scanning Electron Microscopy Images of (a) Ag_2CO_3 (24000 X), (b) Ag_2CO_3 (100,000 X), (c) Pure Halloysite Nanotubes, (d) Ag_2CO_3-50 wt.% HNTs), (e) EDX Mapping of Ag_2CO_3-HNTs and (f) EDX Spectrum of Ag_2CO_3-HNTs.
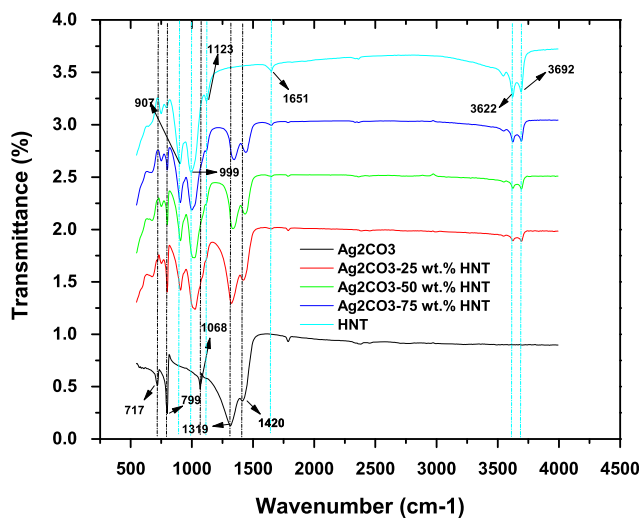

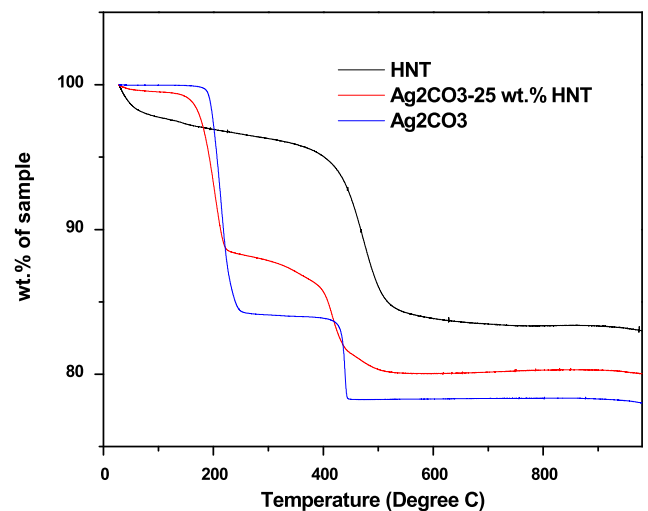**Fig. 3.** FTIR spectra for Ag_2CO_3, HNTs and Ag_2CO_3-HNTs.

Fig. 4. The thermogravimetric analysis of HNTs, Ag_2CO_3 and Ag_2CO_3-HNTs.
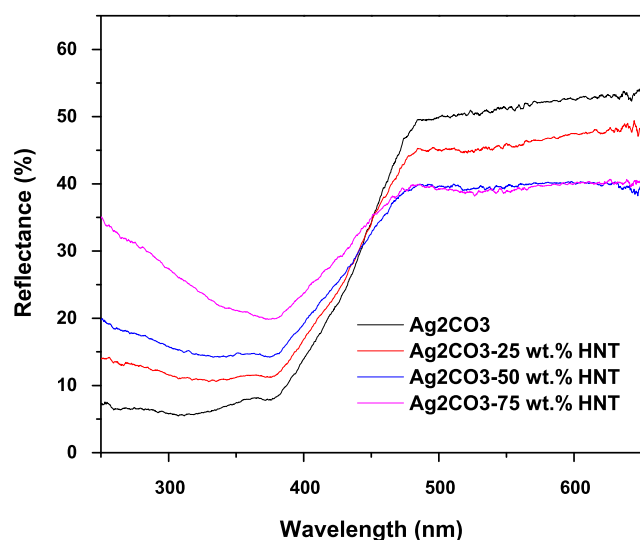
Fig. 5. DRS spectra of Ag_2CO_3 and Ag_2CO_3-HNTs.

Table 1
Optical band gap energies estimated from the Kubleka-Munk method.

Photocatalyst	Optical Band Gap, eV
Ag_2CO_3	2.50
Ag_2CO_3-25 wt.% HNTs	2.43
Ag_2CO_3-50 wt.% HNTs	2.43
Ag_2CO_3-75 wt.% HNTs	2.43

3.2. Photodegradation of water soluble dyes

The photodegradation efficiencies of Ag_2CO_3 and Ag_2CO_3-HNTs on water soluble dyes were investigated under visible light irradiation (Fig. 6). The concentration of the Ag_2CO_3-HNTs in the dye solution was 1 g/L. This catalyst concentration is less than others reported in literature [43, 44]. Rhodamine b is stable under visible light irradiation hence no degradation occurred under visible light without a photocatalyst. The photocatalyst and dye solution was left in the dark while stirring. This was done to attain adsorption-desorption equilibrium. As can be seen in Fig. 6, significant amount of the dye was adsorbed. The first set of experiments conducted involved using only Ag_2CO_3 at basic and neutral pH. The quantity of rhodamine b dye adsorbed by the Ag_2CO_3 increased when the pH was decreased from 9.34 to 7 (Fig. 6(a)). In addition, the photocatalytic activity of Ag_2CO_3 was significantly higher at neutral pH than basic pH. The removal efficiency and the first order rate constant

were estimated as 75 % and 0.0547 min^{-1}, and 83 % and 0.0965 min^{-1} at pH of 9.34 and 7, respectively (Fig. 6 (b)). The photocatalytic activity is therefore dependent on the pH of the dye solution. It has been reported that, the surface charge characteristics of Ag_2CO_3 depends on the starting pH of the aqueous medium in which the photocatalysis is taking place [45, 46]. The change in the surface charge characteristics of the Ag_2CO_3 at basic pH resulted in the Ag_2CO_3 repelling the rhodamine b dye and this is seen in the reduced adsorption of rhodamine b dye by Ag_2CO_3 (Fig. 6). For enhanced photocatalytic activity, the dye must be adsorbed onto the surface of the Ag_2CO_3. It is therefore not surprising that the pH that recorded the least adsorption of the dye also recorded the least photocatalytic activity. Another possible explanation for the variation in the photodegradation efficiency with pH is that Ag based semiconductors are unstable in solution of basic and acidic pH and this influenced the degradation of the rhodamine B dye [47].

From Fig. 6, Ag_2CO_3-HNTs recorded a higher adsorption and photocatalytic activity than pure Ag_2CO_3. The dye removal efficiency and pseudo first order rate constant increased from 83 % and 0.0965 min^{-1} for Ag_2CO_3 at neutral pH to 97 % and 0.2683 min^{-1} for Ag_2CO_3-75 wt.% HNTs. The removal efficiency and the rate constant increased as the amount HNTs in the Ag_2CO_3-HNTs composite increased. The surface of HNTs has been reported to be slightly negative above the pH of 2.7 [22] and as a result attracted the cationic rhodamine b. This explains the enhanced adsorption and degradation of rhodamine B by Ag_2CO_3-HNTs. In addition, HNTs are highly dispersed in aqueous solution. It was observed that the Ag_2CO_3-HNTs remained dispersed even without stirring when conducting the photocatalysis test while the Ag_2CO_3 quickly settled. The improved photodegradation efficiency of Ag_2CO_3-HNTs may be ascribed to its enhanced dispersity in aqueous solution.

As already discussed above, the photodegradation efficiency was influenced by pH. The authors investigated the effect of pH on the photodegradation activity of the composite using Ag_2CO_3-25 wt.% HNTs and the results presented in Fig. 7. The least pseudo first order rate constants were observed at lower pH (Fig. 7). Ag_2CO_3 has been reported to dissolve in acidic solution [48]. It is there possible that, in acidic pH, the structure of Ag_2CO_3 was disrupted destroying its photocatalytic activity.

To ensure that the composite Ag_2CO_3-HNTs can photodegrade other dyes, photocatalysis test was done on methylene blue dye using Ag_2CO_3 and Ag_2CO_3-25 wt.% HNTs (Figs. 7 and 8). The degradation of methylene blue was pronounced for Ag_2CO_3-25 wt.% HNTs compared to that of Ag_2CO_3 (Fig. 8A). The removal efficiency and the pseudo first order rate constant of Ag_2CO_3 and Ag_2CO_3-25 wt.% HNTs were calculated to be 63 % and 0.0251 min^{-1}, and 93 % and 0.0286 min^{-1}, respectively. One notable observation was the drastic reduction in the amount of the methylene blue dye after the 30 minutes of stirring in the dark to attain adsorption-desorption equilibrium. Our previous studies concluded that clay samples easily adsorb methylene blue than rhodamine b dye due to
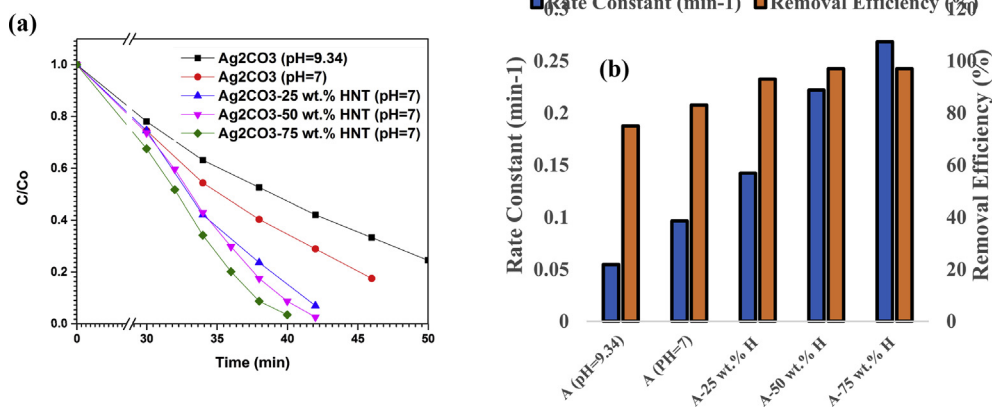

Fig. 6. (a) Photodegradation of rhodamine b dye by Ag_2CO_3 and Ag_2CO_3-HNTs (b) Calculated removal efficiencies and first order rate constant (k) of Ag_2CO_3 and Ag_2CO_3-HNTs [A = Ag_2CO_3, H=HNTs].
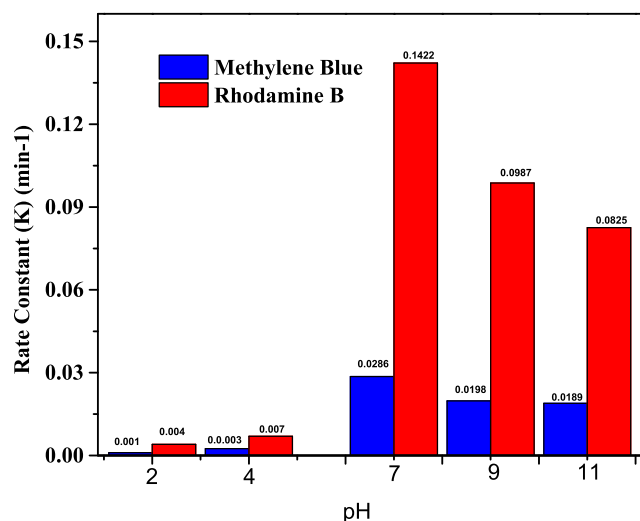
Fig. 7. Effect of pH on the photodegradation of rhodamine b and methylene blue (Ag$_2$CO$_3$-25 wt.% HNTs).

the difference in molecular structure and ionic charge characteristics of these two dyes [49].
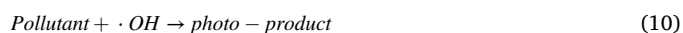
Based on the observation in Fig. 8, the authors decided to conduct a detailed adsorption studies on Ag$_2$CO$_3$-50 wt.% HNTs composite using methylene blue since it became obvious that the removal of the dye solution is due to a combination of photocatalysis and adsorption. The adsorption of methylene blue is due to the interaction between the anionic surface of HNTs and the positively charged methylene blue.

The reusability of Ag$_2$CO$_3$-HNTs was also investigated (Fig. 9). The photodegradation activity reduced from ca. 93 % to ca. 64 % upon reusing the Ag$_2$CO$_3$-25 wt.% HNTs on five consecutive cycles. Generally, Ag based photocatalysts are unstable due to photo corrosion. Ag$_2$CO$_3$ is moderately soluble in aqueous solution (solubility product constant of 8.3×10^{-12}). The Ag$^+$ may react with photogenerated electrons and transform to metallic Ag [50]. Over time, more of the silver in Ag$_2$CO$_3$ will be converted into metallic silver. This is responsible for its instability during photocatalysis. Subsequently, the photocatalytic activity will reduce, rendering the Ag$_2$CO$_3$-HNTs non-usable.

Superoxide and hydroxyl radicals, and photogenerated holes are the reactive oxygen species (ROS) responsible for the photodegradation of dyes. Scavengers such as isopropanol, DMSO, ethylenediamine teraacetic acid disodium salt (EDTA-2Na) and benzoquinone (BQ), have been employed to determine the reactive species responsible for the photo-degradation of dyes [33, 51]. BQ, DMSO and EDTA-2Na have been

employed as scavengers for holes (h^+), $\cdot OH$, and $\cdot O_2^-$, respectively. DMSO, BQ and EDTA-2Na were used to examine the reactive species (RS) responsible for the photodegradation of methylene blue dye. Fig. 10 represents the results for the free radical experiment. DMSO and BQ had little effect on the photodegradation of methylene blue. The degradation efficiency recorded without the addition of a scavenger was 93 %. Upon the addition of BQ and DMSO, the degradation efficiency reduced to 79 and 81 %, respectively. This implies that, the major RS is h^+ and not $\cdot OH$ and $\cdot O_2^-$. To confirm this, EDTA-2Na which is a h^+ scavenger was added. After the addition of EDTA-2Na, the photodegradation efficiency reduced to 27 %. This suggest that, photogenerated holes (h^+) are the major RS, responsible for the photodegradation of methylene blue. This result agrees with already reported findings which revealed that photo-generated holes are the main RS responsible for the degradation of methylene blue by Ag$_2$CO$_3$ [33]. This suggests that, the formation of RS for the photodegradation of methylene blue by the composite Ag$_2$CO$_3$-HNTs was controlled by Ag$_2$CO$_3$.

The possible photoreaction equations taking place are summarized in the equations below:

$$Ag_2CO_3 - HNTs \xrightarrow{h\nu} h^+ + e^- \tag{3}$$

$$O_2 + e^- \rightarrow \cdot O_2^- \tag{4}$$

$$\cdot O_2^- + 2H^+ + e^- \rightarrow H_2O_2 \tag{5}$$

$$H_2O_2 + e^- \rightarrow \cdot OH + OH^- \tag{6}$$

$$OH^- + h^+ \rightarrow \cdot OH \tag{7}$$

$$H_2O + h^+ \rightarrow \cdot OH + H^+ \tag{8}$$

$$Pollutant + \cdot O_2^- \rightarrow photo - product \tag{9}$$

$$Pollutant + \cdot OH \rightarrow photo - product \tag{10}$$

$$Pollutant + h^+ \rightarrow photo - product \tag{11}$$

A proposed mechanism for the photodegradation of Ag$_2$CO$_3$-HNTs is presented schematically in Fig. 11. When visible light is absorbed, electrons are transferred from the conduction band (CB) to the valence band (VB). This leads to the creation of electron-hole pair (equation 3). The intimate contact between the Ag$_2$CO$_3$ and the HNTs allows for efficient delocalization of photogenerated electrons by the electrical conductance between the HNTs and Ag$_2$CO$_3$ due to the high electrical conductance of nanoclays [52]. This is expected to reduce the electron-hole
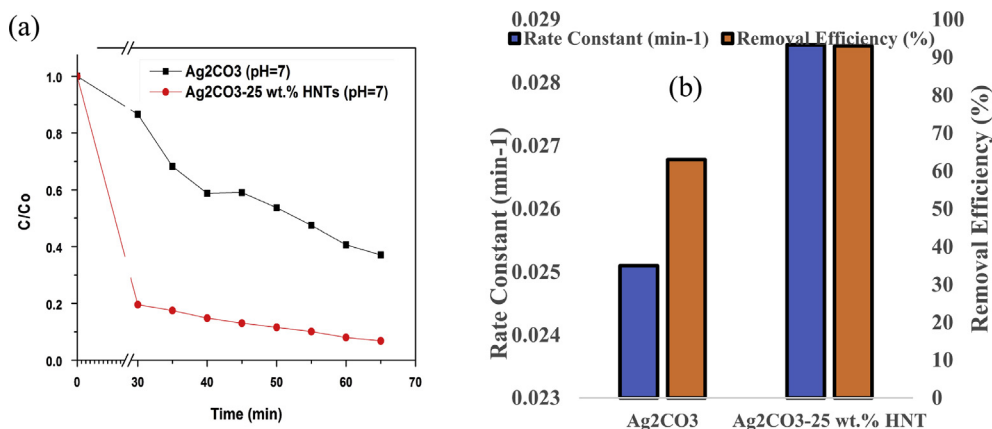

Fig. 8. (a) Photodegradation of methylene blue by Ag$_2$CO$_3$ and Ag$_2$CO$_3$-25 wt.% HNTs, (b) Calculated pseudo first order rate constants and removal efficiencies by Ag$_2$CO$_3$ and Ag$_2$CO$_3$-25 wt.% HNTs.
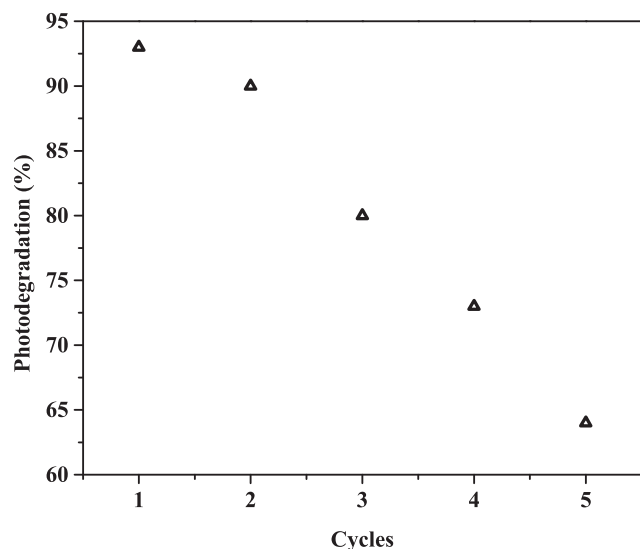
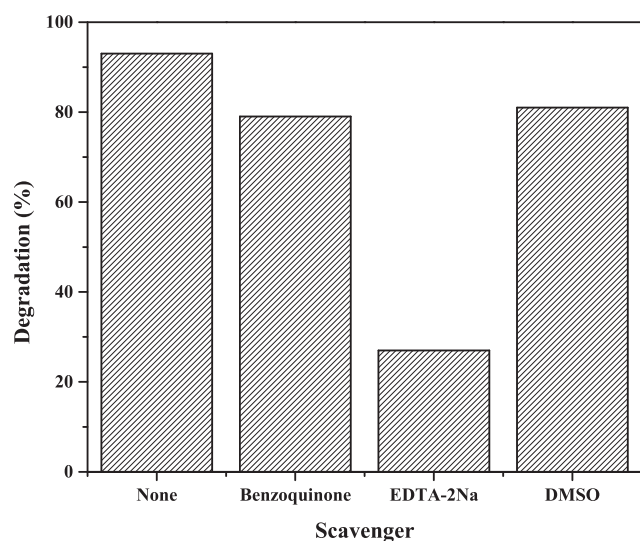**Fig. 9.** Reusability of Ag_2CO_3-25 wt.% HNTs.

Fig. 10. Effect of scavengers on the photocatalytic degradation of methylene blue (Ag_2CO_3-25 wt.% HNTs).

recombination resulting in an increase concentration of holes in the Ag_2CO_3 and electrons in the HNTs. The photogenerated holes oxidize the dye pollutants generating photoproducts. On the other hands, the electrons trapped in the HNTs can attack dissolve oxygen molecules and result in the generating of ROS. In the absence of HNTs, most of the photogenerated holes may combine with the photogenerated electrons reducing the photocatalytic activity. The results from the free radical experiment implies that, photogenerated holes are the specie responsible for the photodegradation of methylene blue dye. The photodegradation of methylene blue therefore occurred by Eqs. (3) and (11). When HNTs are not present, the generated holes and electrons may recombine. This phenomenon known as electron-hole recombination will decrease photocatalytic activity as observed in Figs. 6, 7, and 8.

3.3. Adsorption characteristics of Ag_2CO_3-HNTs

To understand the adsorption characteristics of Ag_2CO_3-HNTs, an adsorption studies was conducted using methylene blue solution and the results presented in Fig. 12 and Table 2. The Ag_2CO_3-HNTs particle concentration was 0.375 g/L. The Langmuir (equ.12) and Freundlich
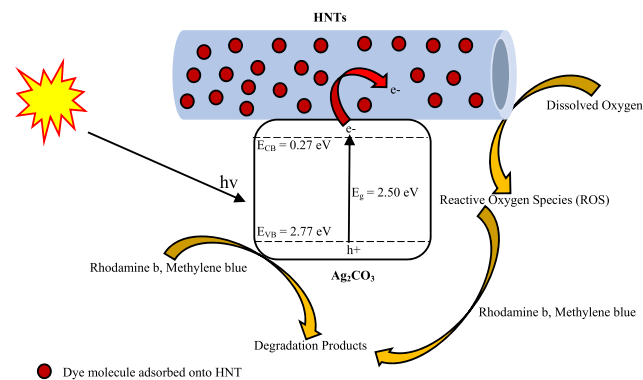

Fig. 11. Schematic diagram for the adsorption and photodegradation of methylene blue and rhodamine B dyes by Ag_2CO_3-HNTs.

(equ.14) equilibrium isotherms were used to examine the adsorption mechanism. The data obtained from the adsorption studies was fitted with the linearized form of the isotherms presented in the equation below;

$$\frac{C_e}{Q_e} = \frac{C_e}{Q_m} + \frac{1}{K_L Q_m} \tag{12}$$

$$R_L = \frac{1}{1 + K_L C_O} \tag{13}$$

$$\ln Q_e = \ln K_F + \frac{1}{n} \ln C_e \tag{14}$$

C_o (mg/L) and C_e (mg/L) represent the initial and equilibrium dye concentrations, respectively. The amount of dye adsorbed on Ag_2CO_3-50 wt.% HNTs at equilibrium and the maximum adsorption capacity are represented by Q_e (mg/g) and Q_m (mg/g), respectively. K_F mg/g (mg/L)$^{1/n}$ and K_L (L/mg) corresponds to the Freundlich and Langmuir constant, respectively. A higher K_F corresponds to a higher adsorption affinity. The adsorption intensity is related to the value of $1/n$. $1/n$ values within the range $0.1 < 1/n < 1$, indicate favorable adsorption [53, 54]. From the Langmuir isotherm equation, the plot of C_e/Q_e vs C_e is presented in Fig. 12(A). K_L and Q_m were estimated from the intercept and slope, respectively and are summarized in Table 2. How favorable the adsorption process is was examined using an equilibrium parameter R_L calculated from equ.13 and the values presented in Table 2. If the R_L is between 0 and 1, it indicates a favorable adsorption process. A R_L value of 0 indicates an irreversible adsorption process. When R_L is 1, the adsorption is linear and is unfavorable when $R_L > 1$. The maximum monolayer adsorption capacity (Q_m) and the equilibrium parameter (R_L) of the Ag_2CO_3-50 wt.% HNTs were calculated to be 13.7287 mg/g and 0.03769–0.16377, respectively. With high correlation coefficient from Fig. 12a, these values imply that the surface of the Ag_2CO_3-50 wt.% HNTs is homogenous and was covered with a monolayer methylene blue dye. In addition, methylene blue adsorption by Ag_2CO_3-50 wt.% HNTs was favorable. Fig. 12(b) was used to calculate the Freundlich constants and presented in Table 2. $1/n$ is less than 1 indicating favorable adsorption process. The K_F and a correlation coefficient (R^2) were estimated as 8.7711 mg/g (mg/L)$^{1/n}$ and 0.8240, respectively. The R^2 for the Langmuir equilibrium isotherm was significantly higher (0.9990) when compared to that of the Freundlich model (0.8240). The adsorption process therefore followed the Langmuir isotherm and confirmed a monolayer adsorption of methylene blue onto Ag_2CO_3-50 wt.% HNTs.

The adsorption process was examined using the pseudo-first order (PFO), pseudo-second order (PSO) and intra-particle diffusion adsorption kinetic models.

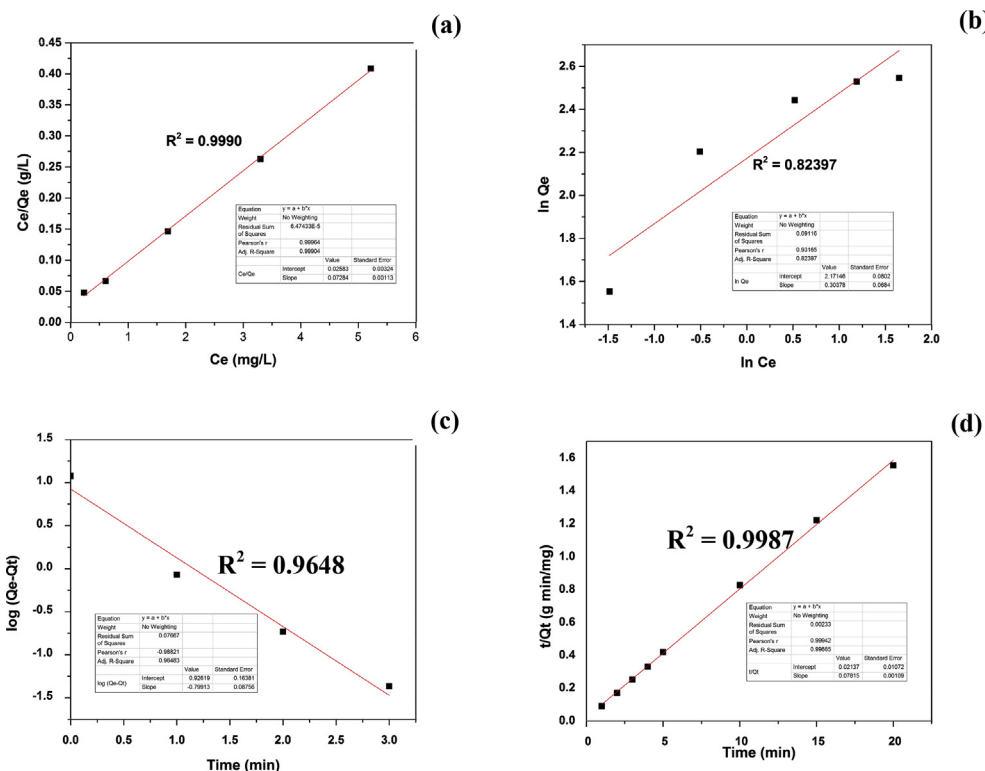The PFO (Eq.15) and PSO (Eq.16) kinetic model are presented below;

Fig. 12. (a) Langmuir Adsorption isotherm, (b) Freundlich adsorption isotherm, (c) First order adsorption kinetics, (d) Second order adsorption kinetics.

Table 2
Adsorption kinetics and equilibrium data for the adsorption of methylene blue unto Ag_2CO_3-50 wt.% HNTs.

Adsorption Kinetic Models	Adsorption Kinetic Parameters
Langmuir	Q_m = 13.72 [error: 0.2097] (mg/g)
	K_L = 2.553 [error: 0.3105] (L/mg)
	R^2 = 0.9990
	R_L = 0.03769–0.1637 (L/mg)
Freundlich	K_F = 8.771 [error: 0.7324] (mg/g $(mg/L)^{1/n}$)
	n = 3.291 [error: 0.6049]
	R^2 = 0.8240
Pseudo First Order	Q_e = 8.437 [error: 2.865] (mg/g)
	K_1 = 4.840 [error: 0.2015] (min^{-1})
	R^2 = 0.9648
Pseudo Second Order	Q_e = 12.79 [error: 0.1760] (mg/g)
	K_2 = 0.2856 [error: 0.008222] (g/mg min)
	R^2 = 0.9987
Interparticle Diffusion Model	K_P = 0.7087 [error: 0.0024] (mg/g min $^{1/2}$)
	R^2 = 0.7818

$$\log(Q_e - Q_t) = \log Q_e - \frac{K_1}{2.303} t \tag{15}$$

$$\frac{t}{Q_t} = \frac{1}{K_2 Q_e^2} + \frac{t}{Q_e} \tag{16}$$

Q_t and Q_e (mg/g) indicate the amount of methylene blue adsorbed by the adsorbent at any time t (min) and at equilibrium, respectively. K_2 (min^{-1}) and K_1 (g/mg min) represent the PSO and the PFO adsorption rate constant, respectively. The parameters K_1 and Q_e obtained from PFO and Q_e and K_2 obtained from the PSO were estimated from Fig. 12 (c) and (d), respectively (Table 2). The correlation coefficient obtained in the PSO ((R^2 = 0.9987) is higher compared to the PFO (R^2 = 0.9648). The high correlation coefficient suggests that the adsorption follows a PSO adsorption kinetics process and therefore inclined towards chemisorption.

The intra-particle diffusion model was used to describe the rate controlling steps of the adsorption process as presented below [55];

$$Q_t = K_p t^{1/2} + C \tag{17}$$

Q_t (mg/g) is the amount of methylene blue dye adsorbed at time t (min), C is the intercept corresponding to the boundary layer thickness and K_p (mg/g min $^{1/2}$) is the intra-particle diffusion rate constant. K_p was estimated from Fig. 13 and presented in Table 2. The plot in Fig. 13 shows a double straight line. The initial stage represents the transportation of the dye to the surface of Ag_2CO_3-50 wt.% HNTs through film diffusion. The first linear part represents an instantaneous fast kinetic adsorption resulting from the entry of methylene blue into the halloysite nanotubes by intra-particle diffusion [22]. The final equilibrium stage is represented
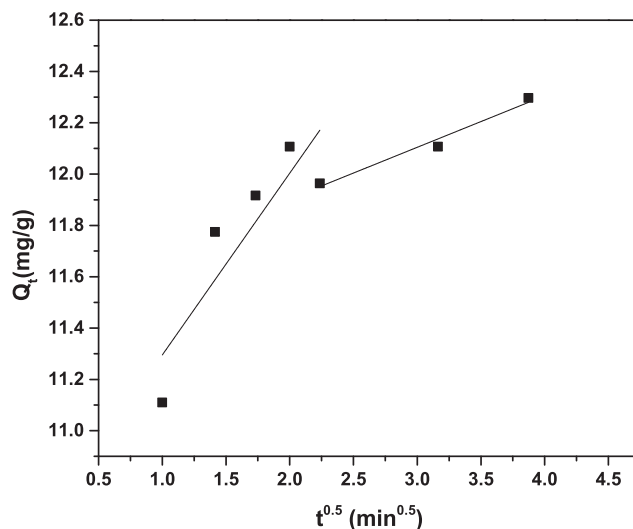

Fig. 13. Interparticle diffusion model for the adsorption of methylene blue unto Ag_2CO_3-50wt.% HNTs.

by the second linear portion of Fig. 13.

The results presented in this paper revealed that Ag$_2$CO$_3$-HNTs has the potential to remove water soluble dye pollutants through adsorption and photocatalysis. Ag$_2$CO$_3$-HNTs therefore has a potential application in the development of water treatment technologies.

4. Conclusions

A photocatalyst-adsorbent composite material made of Ag$_2$CO$_3$ and halloysite nanotubes (HNTs) was synthesized. SEM images showed an intimate contact between the Ag$_2$CO$_3$ and the HNTs. FTIR analysis revealed a shift in the CO_3^{2-} bands to higher wavenumbers and a corresponding shift in the Si–O–Si vibrational band. This implies that the CO_3^{2-} in Ag$_2$CO$_3$ and the Si–O–Si present in the HNTs underwent some level of interaction with each other. The TGA analysis on the other hand showed a multi stage thermal decomposition of Ag$_2$CO$_3$-HNTs. UV-vis DRS analysis and optical band gap estimation revealed an absorption threshold at ca. 480 nm. The HNTs did not have significant effect on the band gap though it influenced the visible and UV light absorption capacity. Ag$_2$CO$_3$-HNTs showed high adsorption capacity and strong photocatalytic activity for both dyes (methylene blue and rhodamine B). It was also observed that, the photocatalytic efficiency was dependent on pH and on the wt.% of HNTs in the Ag$_2$CO$_3$-HNTs and increased with increasing wt.% of HNTs. The electrical conductance between HNTs and Ag$_2$CO$_3$, did not only increased its photocatalytic activity but also improved the aqueous dispersity of Ag$_2$CO$_3$-HNTs composite as compared to the pure Ag$_2$CO$_3$. Photogenerated holes were the major RS responsible for the photodegradation of methylene blue by the Ag$_2$CO$_3$-HNTs composite. The pseudo second order kinetics models and the Langmuir isotherm excellently described the mechanism of the adsorption process. Ag$_2$CO$_3$-HNTs therefore removes dye pollutants by both photocatalytic and adsorption process. This study confirmed the potential application of Ag$_2$CO$_3$-HNTs in water treatment technologies.

Declarations

Author contribution statement

Emmanuel Nyankson: Conceived and designed the experiments; Performed the experiments; Wrote the paper.

Benjamin Agyei-Tuffour: Conceived and designed the experiments; Analyzed and interpreted the data.

Ebenezer Annan: Analyzed and interpreted the data.

Abu Yaya & Bismark Mensah: Analyzed and interpreted the data; Contributed reagents, materials, analysis tools or data.

Boateng Onwona-Agyeman: Conceived and designed the experiments; Contributed reagents, materials, analysis tools or data.

Reuben Amedalor & Benson Kwaku-Frimpong: Performed the experiments.

Johnson Kwame Efavi: Analyzed and interpreted the data; Wrote the paper.

Competing interest statement

The authors declare no conflict of interest.

Additional information

No additional information is available for this paper.

References

[1] M.T. Yagub, T.K. Sen, S. Afroze, H.M. Ang, Dye and its removal from aqueous solution by adsorption: a review, Adv. Colloid Interface Sci. 209 (2014) 172–184.

[2] Y.C. Wong, Y.S. Szeto, W. Cheung, G. McKay, Adsorption of acid dyes on chitosan—equilibrium isotherm analyses, Process Biochem. 39 (6) (2004) 695–704.

[3] V.K. Gupta, Application of low-cost adsorbents for dye removal–a review, J. Environ. Manag. 90 (8) (2009) 2313–2342.

[4] E. Nyankson, D. Rodene, R.B. Gupta, Advancements in crude oil spill remediation research after the Deepwater Horizon oil spill, Water, Air, Soil Pollut. 227 (1) (2016) 29.

[5] K. Shankar, K.C. Tep, G.K. Mor, C.A. Grimes, An electrochemical strategy to incorporate nitrogen in nanostructured TiO2 thin films: modification of bandgap and photoelectrochemical properties, J. Phys. D Appl. Phys. 39 (11) (2006) 2361.

[6] Z. Frontistis, M. Antonopoulou, A. Petala, D. Venieri, I. Konstantinou, D.I. Kondarides, D. Mantzavinos, Photodegradation of ethyl paraben using simulated solar radiation and Ag3PO4 photocatalyst, J. Hazard Mater. 323 (2017) 478–488.

[7] M. Yang, Q. Yang, J. Zhong, S. Huang, J. Li, J. Song, C. Burda, Enhanced photocatalytic performance of Ag2O/BiOF composite photocatalysts originating from efficient interfacial charge separation, Appl. Surf. Sci. 416 (2017) 666–671.

[8] P. Wang, C. Yu, J. Ding, X. Wang, H. Yu, Facile synthesis and improved photocatalytic performance of Ag-AgCl photocatalyst by loading basic zinc carbonate, J. Alloy. Comp. 752 (2018) 238–246.

[9] S. Zhang, H. Zhang, S. Wang, L. Liu, S. Liu, Singlet oxygen formation in bio-inspired synthesis of a hollow Ag@ AgBr photocatalyst for microbial and chemical decontamination, Catal. Sci. Technol. 7 (19) (2017) 4355–4360.

[10] X. Zhao, Y. Su, X. Qi, X. Han, A facile method to prepare novel Ag2O/Ag2CO3 three-dimensional hollow hierarchical structures and their water purification function, ACS Sustain. Chem. Eng. 5 (7) (2017) 6148–6158.

[11] H. Tang, S. Chang, G. Tang, W. Liang, AgBr and g-C3N4 co-modified Ag2CO3 photocatalyst: a novel multi-heterostructured photocatalyst with enhanced photocatalytic activity, Appl. Surf. Sci. 391 (2017) 440–448.

[12] G. Panthi, M. Park, S.J. Park, H.Y. Kim, PAN electrospun nanofibers reinforced with Ag 2 CO 3 nanoparticles: highly efficient visible light photocatalyst for photodegradation of organic contaminants in waste water, Macromol. Res. 23 (2) (2015) 149–155.

[13] C.J. Ward, S. Song, E.W. Davis, Controlled release of tetracycline–HCl from halloysite–polymer composite films, J. Nanosci. Nanotechnol. 10 (10) (2010) 6641–6649.

[14] M. Liu, B. Guo, M. Du, X. Cai, D. Jia, Properties of halloysite nanotube–epoxy resin hybrids and the interfacial reactions in the systems, Nanotechnology 18 (45) (2007) 455703.

[15] V.A. Drits, B.A. Sakharov, S. Hillier, Phase and structural features of tubular halloysite (7 Å), Clay Miner. 53 (4) (2018) 691–720.

[16] E. Nyankson, O. Olasehinde, V.T. John, R.B. Gupta, Surfactant-loaded halloysite clay nanotube dispersants for crude oil spill remediation, Ind. Eng. Chem. Res. 54 (38) (2015) 9328–9341.

[17] G. Cavallaro, L. Chiappisi, P. Pasbakhsh, M. Gradzielski, G. Lazzara, A structural comparison of halloysite nanotubes of different origin by Small-Angle Neutron Scattering (SANS) and Electric Birefringence, Appl. Clay Sci. 160 (2018) 71–80.

[18] E.G. Bediako, E. Nyankson, D. Dodoo-Arhin, B. Agyei-Tuffour, D. Łukowiec, B. Tomiczek, A. Yaya, J.K. Efavi, Modified halloysite nanoclay as a vehicle for sustained drug delivery, Heliyon 4 (7) (2018), e00689.

[19] O. Owoseni, E. Nyankson, Y. Zhang, S.J. Adams, J. He, G.L. McPherson, A. Bose, R.B. Gupta, V.T. John, Release of surfactant cargo from interfacially-active halloysite clay nanotubes for oil spill remediation, Langmuir 30 (45) (2014) 13533–13541.

[20] O. Owoseni, E. Nyankson, Y. Zhang, D.J. Adams, J. He, L. Spinu, G.L. McPherson, A. Bose, R.B. Gupta, V.T. John, Interfacial adsorption and surfactant release characteristics of magnetically functionalized halloysite nanotubes for responsive emulsions, J. Colloid Interface Sci. 463 (2016) 288–298.

[21] Y. Zhao, E. Abdullayev, A. Vasiliev, Y. Lvov, Halloysite nanotubule clay for efficient water purification, J. Colloid Interface Sci. 406 (2013) 121–129.

[22] P. Luo, Y. Zhao, B. Zhang, J. Liu, Y. Yang, J. Liu, Study on the adsorption of Neutral Red from aqueous solution onto halloysite nanotubes, Water Res. 44 (5) (2010) 1489–1497.

[23] R. Liu, B. Zhang, D. Mei, H. Zhang, J. Liu, Adsorption of methyl violet from aqueous solution by halloysite nanotubes, Desalination 268 (1-3) (2011) 111–116.

[24] M. Zhao, P. Liu, Adsorption behavior of methylene blue on halloysite nanotubes, Microporous Mesoporous Mater. 112 (1-3) (2008) 419–424.

[25] G. Cavallaro, I. Grillo, M. Gradzielski, G. Lazzara, Structure of hybrid materials based on halloysite nanotubes filled with anionic surfactants, J. Phys. Chem. C 120 (25) (2016) 13492–13502.

[26] W. Jinhua, Z. Xiang, Z. Bing, Z. Yafei, Z. Rui, L. Jindun, C. Rongfeng, Rapid adsorption of Cr (VI) on modified halloysite nanotubes, Desalination 259 (1-3) (2010) 22–28.

[27] K. Zhu, Y. Duan, F. Wang, P. Gao, H. Jia, C. Ma, C. Wang, Silane-modified halloysite/Fe3O4 nanocomposites: simultaneous removal of Cr (V) and positive effects of Cr (VI) on Sb (V) adsorption, Chem. Eng. J. 311 (2017) 236–246.

[28] M. Fayazi, M.A. Taher, D. Afzali, A. Mostafavi, Fe3O4 and MnO2 assembled on halloysite nanotubes: a highly efficient solid-phase extractant for electrochemical detection of mercury (II) ions, Sensor. Actuator. B Chem. 228 (2016) 1–9.

[29] C. Yu, L. Wei, J. Chen, Y. Xie, W. Zhou, Q. Fan, Enhancing the photocatalytic performance of commercial TiO2 crystals by coupling with trace narrow-band-gap Ag2CO3, Ind. Eng. Chem. Res. 53 (14) (2014) 5759–5766.

[30] X. Yao, X. Liu, One-pot synthesis of ternary Ag2CO3/Ag/AgCl photocatalyst in natural geothermal water with enhanced photocatalytic activity under visible light irradiation, J. Hazard Mater. 280 (2014) 260–268.

[31] H. Wang, J. Li, P. Huo, Y. Yan, Q. Guan, Preparation of Ag2O/Ag2CO3/MWNTs composite photocatalysts for enhancement of ciprofloxacin degradation, Appl. Surf. Sci. 366 (2016) 1–8.

[32] J.M. Falcón, T. Sawczen, I.V. Aoki, Dodecylamine-loaded halloysite nanocontainers for active anticorrosion coatings, Front. Mater. 2 (2015) 69.

[33] H. Dong, G. Chen, J. Sun, C. Li, Y. Yu, D. Chen, A novel high-efficiency visible-light sensitive Ag2CO3 photocatalyst with universal photodegradation performances: simple synthesis, reaction mechanism and first-principles study, Appl. Catal. B Environ. 134 (2013) 46–54.

[34] H. Xu, Y. Song, Y. Song, J. Zhu, T. Zhu, C. Liu, D. Zhao, Q. Zhang, H. Li, Synthesis and characterization of gC 3 N 4/Ag 2 CO 3 with enhanced visible-light photocatalytic activity for the degradation of organic pollutants, RSC Adv. 4 (65) (2014) 34539–34547.

[35] J. Ouyang, D. Mu, Y. Zhang, H. Yang, Mineralogy and physico-chemical data of two newly discovered halloysite in China and their contrasts with some typical minerals, Minerals 8 (3) (2018) 108.

[36] J. Ouyang, B. Guo, L. Fu, H. Yang, Y. Hu, A. Tang, H. Long, Y. Jin, J. Chen, J. Jiang, Radical guided selective loading of silver nanoparticles at interior lumen and out surface of halloysite nanotubes, Mater. Des. 110 (2016) 169–178.

[37] S. Sohrabnezhad, A. Pourahmad, M.M. Moghaddam, A. Sadeghi, Study of antibacterial activity of Ag and Ag2CO3 nanoparticles stabilized over montmorillonite, Spectrochim. Acta Mol. Biomol. Spectrosc. 136 (2015) 1728–1733.

[38] C. Yu, G. Li, S. Kumar, K. Yang, R. Jin, Phase transformation synthesis of novel Ag2O/Ag2CO3 heterostructures with high visible light efficiency in photocatalytic degradation of pollutants, Adv. Mater. 26 (6) (2014) 892–898.

[39] G. Cavallaro, G. Lazzara, S. Milioto, F. Parisi, V. Sanzillo, Modified halloysite nanotubes: nanoarchitectures for enhancing the capture of oils from vapor and liquid phases, ACS Appl. Mater. Interfaces 6 (1) (2013) 606–612.

[40] A.B. Murphy, Band-gap determination from diffuse reflectance measurements of semiconductor films, and application to photoelectrochemical water-splitting, Sol. Energy Mater. Sol. Cell. 91 (14) (2007) 1326–1337.

[41] R. López, R. Gómez, Band-gap energy estimation from diffuse reflectance measurements on sol–gel and commercial TiO 2: a comparative study, J. Sol. Gel Sci. Technol. 61 (1) (2012) 1–7.

[42] G. Dai, J. Yu, G. Liu, A new approach for photocorrosion inhibition of Ag2CO3 photocatalyst with highly visible-light-responsive reactivity, J. Phys. Chem. C 116 (29) (2012) 15519–15524.

[43] R. Jain, M. Mathur, S. Sikarwar, A. Mittal, Removal of the hazardous dye rhodamine B through photocatalytic and adsorption treatments, J. Environ. Manag. 85 (4) (2007) 956–964.

[44] D. Kanakaraju, J. Kockler, C.A. Motti, B.D. Glass, M. Oelgemöller, Titanium dioxide/zeolite integrated photocatalytic adsorbents for the degradation of amoxicillin, Appl. Catal. B Environ. 166 (2015) 45–55.

[45] M. Azami, M. Haghighi, S. Allahyari, Sono-precipitation of Ag2CrO4-C composite enhanced by carbon-based materials (AC, GO, CNT and C3N4) and its activity in photocatalytic degradation of acid orange 7 in water, Ultrason. Sonochem. 40 (2018) 505–516.

[46] H. Salari, A. Daliri, M.R. Gholami, Graphitic carbon nitride/reduced graphene oxide/silver oxide nanostructures with enhanced photocatalytic activity in visible light, Phys. Chem. Res. 6 (4) (2018) 729–740.

[47] G. Li, X. Nie, J. Chen, Q. Jiang, T. An, P.K. Wong, H. Zhang, H. Zhao, H. Yamashita, Enhanced visible-light-driven photocatalytic inactivation of Escherichia coli using g-C3N4/TiO2 hybrid photocatalyst synthesized using a hydrothermal-calcination approach, Water Res. 86 (2015) 17–24.

[48] A. Zhang, L. Zhang, Q. Zhu, B. Dai, W. Sheng, S. Su, J. Xiang, Photocatalytic oxidation removal of Hg0 by ternary Ag@ AgCl/Ag2CO3 hybrid under fluorescent light, Fuel Process. Technol. 159 (2017) 222–231.

[49] E. Nyankson, J.K. Efavi, A. Yaya, G. Manu, K. Asare, J. Daafuor, R.Y. Abrokwah, Synthesis and characterisation of zeolite-A and Zn-exchanged zeolite-A based on natural aluminosilicates and their potential applications, Cogent Eng. 5 (1) (2018) 1440480.

[50] C. Dong, K.L. Wu, X.W. Wei, X.Z. Li, L. Liu, T.H. Ding, J. Wang, Y. Ye, Synthesis of graphene oxide–Ag 2 CO 3 composites with improved photoactivity and anti-photocorrosion, CrystEngComm 16 (4) (2014) 730–736.

[51] A. Zhang, L. Zhang, H. Lu, G. Chen, Z. Liu, J. Xiang, L. Sun, Facile synthesis of ternary Ag/AgBr-Ag2CO3 hybrids with enhanced photocatalytic removal of elemental mercury driven by visible light, J. Hazard Mater. 314 (2016) 78–87.

[52] L. You-ji, C. Wei, Photocatalytic degradation of Rhodamine B using nanocrystalline TiO 2–zeolite surface composite catalysts: effects of photocatalytic condition on degradation efficiency, Catal. Sci. Technol. 1 (5) (2011) 802–809.

[53] V.K. Gupta, C.K. Jain, I. Ali, S. Chandra, S.J.W.R. Agarwal, Removal of lindane and malathion from wastewater using bagasse fly ash—a sugar industry waste, Water Res. 36 (10) (2002) 2483–2490.

[54] A.S. Özcan, B. Erdem, A. Özcan, Adsorption of Acid Blue 193 from aqueous solutions onto Na–bentonite and DTMA–bentonite, J. Colloid Interface Sci. 280 (1) (2004) 44–54.

[55] M. Doğan, M. Alkan, A. Türkyilmaz, Y. Özdemir, Kinetics and mechanism of removal of methylene blue by adsorption onto perlite, J. Hazard Mater. 109 (1-3) (2004) 141–148.